Potential-Dependent Infrared Absorption Spectroscopy of Adsorbed CO and X-ray Photoelectron Spectroscopy of Arc-Melted Single-Phase Pt, PtRu, PtOs, PtRuOs, and Ru Electrodes

ARTICLE · MARCH 2000

DOI: 10.1021/jp992943s

Potential-Dependent Infrared Absorption Spectroscopy of Adsorbed CO and X-ray Photoelectron Spectroscopy of Arc-Melted Single-Phase Pt, PtRu, PtOs, PtRuOs, and Ru Electrodes

Renxuan Liu, Hakim Iddir, Qinbai Fan, Gouyan Hou, Aili Bo, Kevin L. Ley, and E. S. Smotkin*

Illinois Institute of Technology, Center for Electrochemical Science and Engineering, Chicago, Illinois 60616

Y.-E. Sung,† H. Kim, S. Thomas, and A. Wieckowski*

University of Illinois at Urbana−Champaign, Department of Chemistry, 505 South Mathews Avenue, Urbana, Illinois

Received: August 19, 1999; In Final Form: February 5, 2000

The potential- and coverage-dependent infrared absorption spectroscopy (IRAS) of linearly bound CO on single-phase polycrystalline arc-melted Pt, PtRu(1/1), PtRu(8/2), PtOs(8/2), PtRuOs(8/1/1), PtRuOs(65/25/10), and Ru electrodes in 0.5 M H_2SO_4 are correlated with the potential-dependent X-ray photoelectron spectroscopy (XPS) of the PtRu(1/1), PtOs(8/2), and PtRuOs(65/25/10) substrates. The CO stretching frequencies decrease as the mole fraction of Pt in the alloy is decreased. The CO oxidation onset on pure Pt at 100.0% CO coverage is 0.5 V vs a reversible hydrogen electrode and shifts negatively as the alloy mole fraction of Pt is reduced. At CO dosing conditions that yield 100% coverage on pure Pt, the CO bandwidths increase with decreasing Pt mole fraction: on pure Pt the bandwidths increase as the CO coverage is reduced. The effects of CO coverage and bulk alloy composition on the Stark tuning rates (STRs) have been systematically examined on Pt, and a series of binary and ternary alloy surfaces. The XPS data confirm a potential-dependent surface distribution of oxides and no significant surface segregation of the alloying components. The systematic displacement, to lower frequencies, of the linear STRs as the mole fraction of Pt is reduced suggests no significant island formation on the arc-melted alloy surfaces. The XPS data also suggest that the alloying metals, rather than Pt, are responsible for activation of the water required for methanol oxidation in the direct methanol fuel cell potential window.

Introduction

Direct oxidation methanol fuel cells (DMFCs) need better anode electrocatalysts than pure Pt, which suffers from self-poisoning phenomena. The four electron oxidative adsorption of methanol yields adsorbed CO (CO_{ads}) which blocks active sites.[1−3] The low activity for CO_{ads} oxidation has been ascribed to an insufficient surface density of adsorbed oxygenated species such as $-OH_{ads}$ or activated water (H_2O_{act}) on Pt at the low potentials required for DMFC performance.[4] The formation of Pt−OH, on pure Pt, occurs in substantial quantities only at potentials greater than 0.8 V, too positive for practical DMFC performance.[23] Recently, Iwasita et al. reported that at high potential (e.g. $\approx$ 0.7 V), the H_2O−Pt interaction competitively hinders adsorption of methanol.[5] Thus at potentials below 0.7 V some form of activated water (H_2O_{act}) is more likely involved in the oxidation of CO on Pt. It is generally accepted that binary or ternary systems such as those based on Pt, Ru, and Os components are much better than Pt as methanol oxidation catalysts.[6−19] PtRu is the most commonly used DMFC anode catalyst[22] prepared in highly dispersed form by the Watanabe[20] or Adams[21] methods. The low solubility in Pt, of key candidate alloying metals as well as the advent of combinatorial screening methods for electrocatalysts, motivates study of ternary, quaternary, and higher-order alloys.

The improved kinetics enabled by promoters such as Ru, Sn, Mo, or Os has been attributed to a bifunctional and/or a ligand (electronic) effect.[8,22−28] In the bifunctional mechanism the second atom enhances reactivity by readily adsorbing some form of active oxygen, thereby increasing the methanol oxidation rate through a bimolecular surface reaction. Ligand effects have been attributed to changes in the electronic state of the Pt, which affects activation of the methanol C−H bond or Pt-adsorbate binding.[23,29,30] If the surface reaction of oxygenated species with CO_{ads} is rate limiting, then a Pt/M ratio near unity should be optimal. Ligand effects may increase the optimal ratio over that expected from the assumption of purely bifunctional effects.

Key issues include the arrangement and speciation of the metal components on the catalytic surface. According to Gasteiger and co-workers, at least three adjacent Pt sites are needed for methanol chemisorption,[31,32] suggesting a surface Pt/Ru ratio greater than unity. In contrast, for oxidation of CO, where chemisorption of the linear CO form requires only a single Pt site, a model for the optimal surface composition for electro-oxidation is 1:1.[33] Whether such compositions can be made may depend on phase equilibria (e.g., single-phase arc-melted PtMo(1/1) cannot be made since the solubility limit of Mo in the Pt fcc lattice is only 20%). The sparse knowledge of the surface structure of methanol anode catalysts leaves open

* Corresponding author.
† Present address: Department of Materials and Engineering, K-JIST, Kwangju 500-712, Korea.

10.1021/jp992943s CCC: $19.00
Published on Web 03/24/2000

many questions concerning catalyst structure/function relationships.[14,34] For instance, while the bulk phase diagram for PtRu is well-known, little is known of surface (2-dimensional) phase diagrams in the PtRu or the ternary systems. In fact, although high-surface-area catalysts prepared by borohydride reduction exhibit only disordered single-phase fcc XRD patterns, our recent study comparing lattice parameters of high-surface-area catalysts to arc-melted alloys of nominally the same composition suggests that at least one additional amorphous phase exists in the high-surface-area catalysts (probably an oxide, rich in the alloying component) in addition to the fcc lattice observed by XRD.[15,35] In addition, our X-ray photoelectron spectroscopy (XPS) data of high-surface-area catalysts are consistent with a crystalline phase observed by XRD, in combination with an oxide phase(s). Rolison points out that oxide surfaces and phases that enhance ionic conductivity of high-surface-area catalysts are advantageous.[36,37] Thus high-surface-area catalysts are more complex than single-phase arc-melted alloys. Summarizing, we observe a single-phase fcc lattice as one of the phases in high-surface-area catalysts and as the only bulk phase in the arc-melted alloys.

Although the role of each phase must be studied, this study focuses on the alloy fcc phases. Quantification and speciation of the alloy components on the surface are required for even a semiquantitative interpretation of potential-dependent infrared absorption spectroscopy (IRAS) of adsorbed CO on alloy surfaces. Another issue is the occurrence of inter-metallic charge transfer in alloy systems. Goodenough et al. suggest that electron transfer from Ru to Pt within the alloy may be responsible for the synergistic promotion of fuel cell reactions.[28] Such electron transfer could contribute additional back-bonding to the $2\pi^*$ molecular orbital of the adsorbed CO. This would be consistent with lowering of the stretching frequencies as the mole fraction of Pt is reduced in Pt-based alloys, as will be discussed later in the paper.

In this work, potential-dependent IRAS and XPS are used to probe PtRu, PtOs, PtRuOs alloy surfaces in sulfuric acid solutions to improve our understanding of the role of the alloying metal(s) in DMFC anodes. IRAS has been widely applied to the study of adsorbed species at electrode/electrolyte interfaces, including CO_{ads} on platinum group metallic electrodes and Pt-based Ru alloy electrodes.[38−42] Ponec has studied the adsorption of carbon monoxide, at open circuit, on Pt alloys supported on γ-alumina[43] including Pt−Pb. Vielstich has studied CO electrooxidation at Pt, Ru, and PtRu(1/1) by FTIR.[44] Previous XPS work is limited and primarily restricted to Pt−Ru binary alloys.[45,46] We have quantified the surface oxidation states of the individual components of binary and ternary arc-melted alloys by XPS, and correlated the XPS to the IRAS of adsorbed CO on the same systems. The comparative FTIR/XPS of these electrodes provides insights concerning DMFC electrooxidation mechanisms.[47] Previously reported investigations in electrocatalysis using UHV spectroscopy have been performed via sample transfer through air, which can result in contamination, possibly altering the adsorbate arrangements on the electrode surface in solution. In UHV-electrochemistry, where exposure of the surface to air is avoided, it is possible to perform both surface and electrochemical characterization under strictly controlled conditions, avoiding artifacts due to the exposure of the electrode surface to air.[48−50]

Experimental Section

Arc-melted polycrystalline Pt, PtRu(1/1), PtRu(8/2), PtOs-(8/2), PtRuOs(8/1/1), PtRuOs(65/25/10), and Ru electrodes were previously prepared and the XRD patterns (Cu Kα) confirm they are all *fcc* single phase,[15] with no supercell lines indicative of ordering of Pt, Ru, and Os.

The UHV-electrochemistry chamber consists of two chambers: the main UHV-chamber where standard methods of electron spectroscopy and vacuum surface preparation are performed, and the antechamber for electrochemical studies. The two chambers are separated by a gate valve, which is closed during electrochemical work. The base pressure of the UHV chamber was maintained at less than 3×10^{-10} Torr. Sample surfaces were cleaned by repeatedly sputtering (1×10^{-5} Torr of Ar^+, 1 keV) and annealing (5 V, 12 A) (sometimes, sputtering only to prevent surface segregation). The sputtering process was continued during the cleaning process until carbon was no longer evident by X-ray photoelectron spectroscopy. The XPS were recorded with Surface Science Instruments M-Probe ESCA system with the high-resolution semispherical capacitor analyzer under fixed analyzer transmission (constant pass energy) mode. The source was a monochromatic Al Kα line (1486.6 eV) with 150 W power and was focused on an area with ~1 mm diameter. As we reported previously[51] (I), all binding energy values were calibrated by referencing Pt 4f lines (79.0 eV) of sputter-cleaned Pt(111).

The electrode was routinely transferred to an air-isolated electrochemical chamber, which was followed by bringing the chamber to atmospheric pressure with ultrapure argon. The alloy surface was contacted to 0.5 M H_2SO_4 (ultrapure grade, Ultrex from VWR with Millipore water (18 MΩ cm) solution for voltammetric characterization and adsorption studies. Solutions were deaerated with nitrogen (Linde, Oxygen Free, 99.99%). The electrochemical measurements were carried out using a conventional three-electrode cell and an EG&G PAR 273 potentiostat. The electrode potentials were measured with respect to a Ag/AgCl (1 M KCl) reference and reported vs the reversible hydrogen electrode (RHE) scale. Following electrochemical treatment, the electrode was rinsed with Ar-saturated solutions, and then the antechamber was pumped down to UHV conditions. The sample was then transferred to the XPS chamber.

The XPS core-level spectra were fitted to the Doniach-Sunjic line shape convoluted by a Gaussian contribution taking into account the spectrometer resolution. Background removal was carried out by using a Shirley baseline method.[52] Both ends of the baseline were set far enough not to distort the shape of spectra, including tails. Small variation of the range of the baseline did not change the relative amount of fitted species (less than 1%). For homogeneous alloys of AB or ABC, a simple linear expression furnishes quantitative results.[53,54] If I_x and I_x^0 are the intensities of a chosen transition on the XPS spectrum of the alloy and the same transition for the pure elements, the surface concentration of the constituent A may be given by

$$C_A = \frac{I_A/I_A^0}{\sum_{x=A,B,C} I_x/I_x^0} \qquad (1)$$

We either experimentally measured the pure element intensities (e.g., pure Pt and thick layer of Ru on Pt) or used literature-value sensitivity factors for Pt 4f, Ru 3d, and Os 4f.[55] This simple relationship permits an estimation of the number of monolayers, not surface coverage. The surface coverage (θ) of ruthenium oxides and osmium oxide on the alloys was determined by XPS using the modified relative ratio method:[54,56]

$$\frac{I_{AO}}{I_{A,sub}} = \frac{n_{AO}}{n_A}\cdot\frac{T_{AO}}{T_A}\cdot\frac{\sigma_{AO}}{\sigma_A}\cdot\frac{\lambda_{AO}}{\lambda_A}\cdot\frac{\theta_{AO}\{1-\exp[-a_{AO}/\lambda_{AO}\cos\alpha]\}}{1-\theta_{AO}\{1-\exp[-a_{AO}/\lambda_{AO.sub}\cos\alpha]\}} \quad (2)$$

where I is the peak intensity, n is the number of atoms of the element per cm^3, T is the transmission function of the spectrometer, σ is the photoionization cross section, λ is the inelastic mean free path, and α is the angle between the sample normal and the direction of the XPS electron beam. The subscripts "sub," AO, and A refer to the substrate, the core levels of the oxide, and the elemental core levels, respectively. The method of Tanuma et al.[57,58] was used to estimate λ.

The IRAS spectro-electrochemical cell is similar to those reported in previous studies.[59,60] A 60° beveled CaF_2 trapezoid window was mounted on a glass flange with a Teflon-coated Viton O-ring. The working electrodes were glued with epoxy onto a glass syringe piston, leaving one side of the crystal exposed as the electrode surface, with the spot-welded Pt wire fed into the interior of the syringe piston for connection to the potentiostat. A platinized Pt wire was used as the counter electrode. The cyclic voltammograms were obtained with a PAR VersaStat. All potentials are referenced to a RHE consisting of a platinized palladium foil in contact with 1 atm H_2 in 0.5 M H_2SO_4.

The electrodes were polished (0.25 μm, diamond paste), ultrasonically cleaned (12 min) in Nanopure water (18.3 MΩ), and quickly transferred into the spectro-electrochemical flow cell. The cell was purged with 0.5 M H_2SO_4 delivered from a reservoir purged with Ar. The Pt electrode was cycled between 0 and 1.4 V vs RHE until a steady-state CV revealed hydrogen adsorption−desorption peaks. The Pt-based alloy electrodes were cycled 20 times between 0 and 0.8 V.[20] Binary Pt−Ru (1:1) alloy surfaces are known to be resistant to Pt-enrichment, caused by preferential Ru dissolution, up to ca. 1 V.[15] The Os-containing alloys in this work were stable up to 0.8 V.[15] Prolonged potential cycling of these electrodes at 100 mV/s to an upper limit of 0.8 V produced no voltammetric features in the hydrogen region characteristic of Pt-enrichment. The potential program used for CO adsorption, after the initial cycling,[61] is identical to that used in our previous work.[15] After cycling, all electrodes were then stepped to −50 mV for 10 s and then to 0.05 V (the dosing adsorption potential). The spectro-electrochemical cell was then purged with 0.1%, 1%, or 50% CO-balanced Ar for 10 min. Oxygen-free 0.5 M H_2SO_4 solution was then flushed through the cell to remove CO from the cell solution. The electrode surface was then pressed up against the CaF_2 window, by movement of the syringe piston, prior to performing the potential-step experiments.

The IRAS experiments were conducted with a Mattson Research Series-II spectrometer configured with an ATI instrument real-time sampling accessory and a MCT detector. The photoelastic modulator (Hinds International ZnSe series PEM-90) frequency is 37 kHz. The polarization modulation experiments involved the alternating acquisition of two interferograms: I_s, the sum interferogram, and I_d, a difference interferogram.

Results

XPS of Arc-Melted Pt/Ru(1/1) Electrode. In Figure 1A the potential-dependent Pt/Ru(1/1) alloy electrode Pt 4f spectra are shown. The Pt $4f_{7/2}$ and $4f_{5/2}$ lines appear at 71.2 and 74.5 eV,

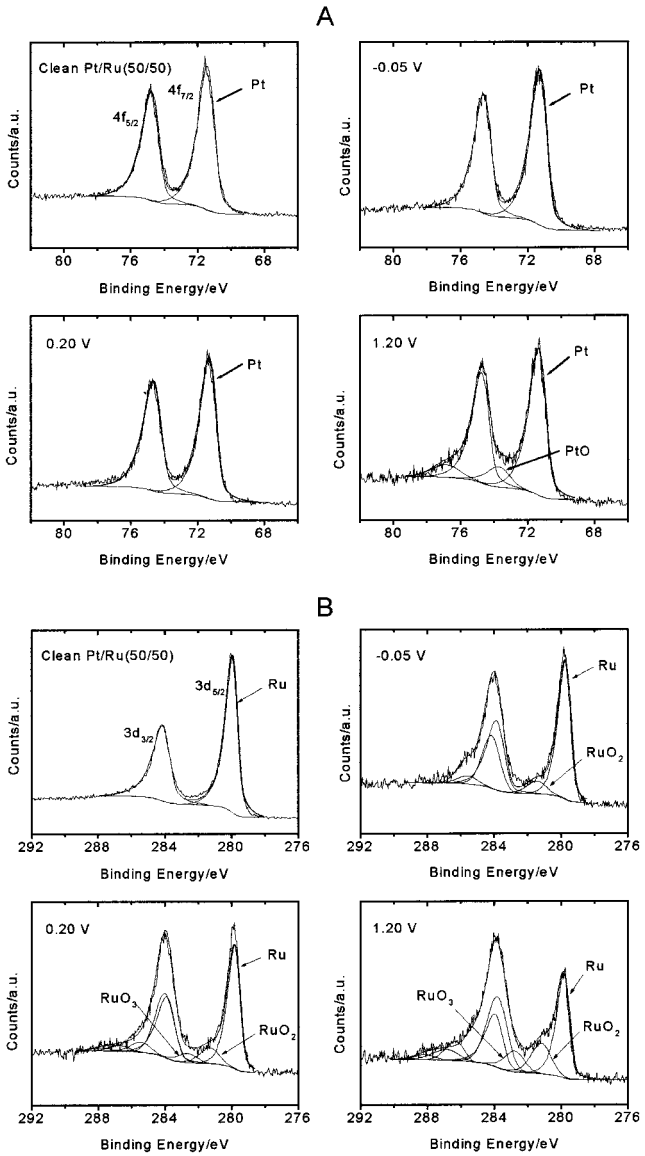

Figure 1. X-ray photoelectron spectra of (A) platinum and (B) ruthenium from the Pt/Ru (50/50) surface at some selected electrode potentials in 0.5 M H_2SO_4. Peak fittings yield spin−orbit-split doublets for platinum and ruthenium. Potentials are given versus a reversible hydrogen electrode (RHE). The source was monochromatic Al Kα line at $h\nu$ = 1486.6 eV, operated at 150 W. The analysis was carried out under fixed analyzer transmission (constant pass energy) mode, with constant pass energy of 25 eV. The size of the incident X-ray beam was 1-mm diameter.

respectively. The ratio of peak areas for the spin−orbit split doublet was 4 to 3, corresponding to the theoretical value. Comparison of the binding energies (BE) with those found for pure Pt indicates that Pt is present in the zero-valent state up to 1.0 V vs RHE. At 1.2 V, peak fitting of the Pt 4f region shows two doublets at 73.5 and 76.8 eV, suggesting the presence of metal oxide species. Comparison of the observed BE with those found for various Pt species suggests that the two species are Pt and PtO.[62−66] It is apparent from Figure 1A, that platinum oxides play a minor role in the transfer of oxygen in a bifunctional mechanism for methanol oxidation on alloy catalysts. Further, Pt spectra show almost identical Pt 4f spectra and have very similar potential-dependent BEs.

The Ru 3d region of PtRu XPS spectra is often obscured by the strong C 1s signal due to surface contamination by carbon. Analysis of the Ru 3p line, free from carbon interference,[67] is

TABLE 1: Binding Energies (eV) of Various Pt, Ru, and Os Species Obtained by X-ray Photoelectron Spectroscopy

		pure Pt	thick Ru on Pt	Pt/Ru (50/50)	Pt/Os (80/20)	Pt/Ru/Os (65/25/10)
Pt	$4f_{7/2}$	71.0		71.2	71.1	71.2
	$4f_{5/2}$	74.3		74.5	74.4	74.5
PtO	$4f_{7/2}$			73.5	73.5	
	$4f_{5/2}$			76.8	76.8	
Ru	$3d_{5/2}$		280.0	279.9		279.9
	$3d_{3/2}$		284.2	284.1		284.1
RuO_2	$3d_{5/2}$			281.2		281.3
	$3d_{3/2}$			285.4		285.5
RuO_3	$3d_{5/2}$			282.7		282.9
	$3d_{3/2}$			286.9		287.1
Os	$4f_{7/2}$				50.4	50.5
	$4f_{5/2}$				53.1	53.2
OsO_2	$4f_{7/2}$				51.9	52.0
	$4f_{5/2}$				54.6	54.7

complicated due to the broad 3p lines, rendering an accurate identification of Ru species by XPS difficult. The newly designed UIUC XPS system has sufficient signal-to-noise ratio in the Ru 3d region, even if C is present (Figure 1B), permitting assignment of Ru peaks after peak fitting. A small amount of carbon, not present during AES measurements,[49,50] appears during prolonged XPS measurement, most likely from the chamber wall, and from the XPS analyzer. The XPS Ru 3d region of metallic ruthenium appears as a spin−orbit doublet at 279.9 eV (Ru $3d_{5/2}$) and 284.1 eV (Ru $3d_{3/2}$). The spectra depend on the immersion potential and provide information on the PtRu electronic structure as a function of potential. Our results confirm the presence of Ru oxide species in the PtRu (1/1) electrode. Ruthenium has been characterized by XPS using the $3d_{5/2}$ and $3d_{3/2}$ peaks located at 280.0 and 284.2 eV, respectively, with 1.5 as their area ratio.[53] As shown in Figure 1B, a noticeable Ru $3d_{5/2}$ peak at 279.9 eV is observed after poising at −0.05 V, along with the emergence of another peak at 281.2 eV. This is consistent with in situ EXAFS data.[68] We obtained the best fit assuming that ruthenium oxide, RuO_2, contributed to the spectra. Upon increasing the potential to 0.20 V, an additional Ru peak was found at 282.7 eV, indicating the formation of a second oxide of ruthenium, RuO_3 (Table 1), but the 279.9 eV component remains dominant (Figure 1B). [69−72] There was no additional change in the Ru surface valency until $E = 1.20$ V. Upon increasing the potential to 1.20 V, the relative intensity of the ruthenium oxide species increased (Figure 2A). Note that platinum was found to be stable at the potentials reported here and was always present in the metallic form (Figure 1A). Using Figure 2A and eq 2, we calculated the surface coverage of Ru oxide species shown in Figure 2B. Less than 50% of the Ru is in the form of RuO_2. Thus less than ∼25% of the surface atoms on the PtRu(1/1) alloy surface exists as RuO_2 at potentials below −0.05 V. At 0.20 V, total 90% of Ru surface is in the form of RuO_2 or RuO_3, which is consistent with previous work data.[69,71,72] Above 0.80 V, all of the surface Ru is oxidized (Figure 2B).

Table 2 gives the ruthenium and platinum surface (monolayer) concentrations, calculated from XPS spectra using eq 1, as a function of the potential for the PtRu(1/1) alloy. Before electrochemistry, the as-prepared alloy surface spectra show a slight enrichment of Pt in comparison to the bulk structure. After sputtering with 2 keV argon ions the slight Pt enrichment persists. Table 2 shows that surface enrichment with Pt increases with increasing potential.

XPS of Arc-Melted PtOs(8/2) Electrode. The XPS core-level spectra of PtOs alloy were also examined. The Pt XPS of the alloy are shown in Figure 3A and appear to be almost identical to Pt 4f spectra of the PtRu system with very similar BE at the potentials studied. Again, Pt oxidation occurs at above 1.0 V (Figure 3A). In Figure 3B 90% of the Os signals are at 50.4 and 53.1 eV, close to that reported for Os metal (50.8 eV).[7,73] At the threshold of hydrogen evolution (−0.05 V), the Os $4f_{7/2}$ BE state at 51.9 eV (a 1.5 eV shift from Os metal) indicates that the surface is already oxidized, to an OsO_2 species.[74,75] Increasing the immersion potential up to 1.20 V did not change the nature of the detected Os species and intensity of Os oxide.

To determine the potential dependence of the observed Os metal and Os oxide, the peak intensities were analyzed for a sequence of exposures in the potential range between −0.05 V to 1.40 V. The results are plotted in Figure 4A and 4B. For both lines, the ratio between osmium metal and oxide remains within the same range. That is, no measurable dependence is found. Unlike Ru oxides, the calculated coverages on PtOs(8:2) of OsO_2, ∼20% vs Os ∼4% are quite low in oxides.

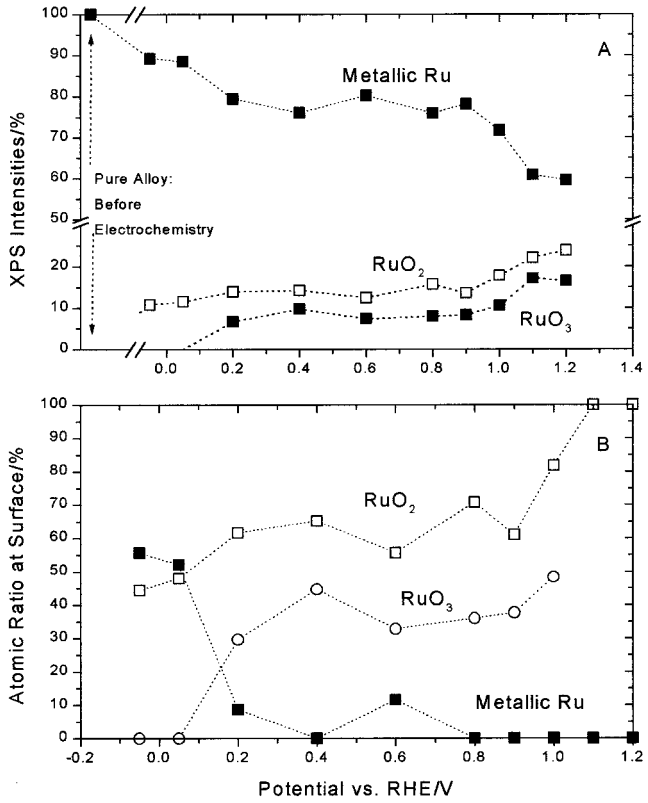

Figure 2. Potential dependency of (A) relative XPS peak intensities from ruthenium species on the Pt/Ru (50/50) surface (from data such as shown in Figure 1), and (B) atomic ratios of ruthenium in different oxidation states. For brevity, the oxidation states are denoted as oxides.

TABLE 2: Atomic Ratio of Pt/Ru (50/50) Alloy at Surface Region vs Electrode Potential

potential (V vs RHE)	Pt (%)	Ru (%)
no potential (before electrochemistry)	51.4	48.6
−0.05	56.5	43.5
0.05	56.8	43.2
0.2	56.4	43.6
0.4	57.4	42.6
0.6	54.6	45.4
0.8	54.2	45.8
0.9	59.6	40.4
1.0	58.2	41.8
1.1	58.2	41.8
1.2	58.1	41.9

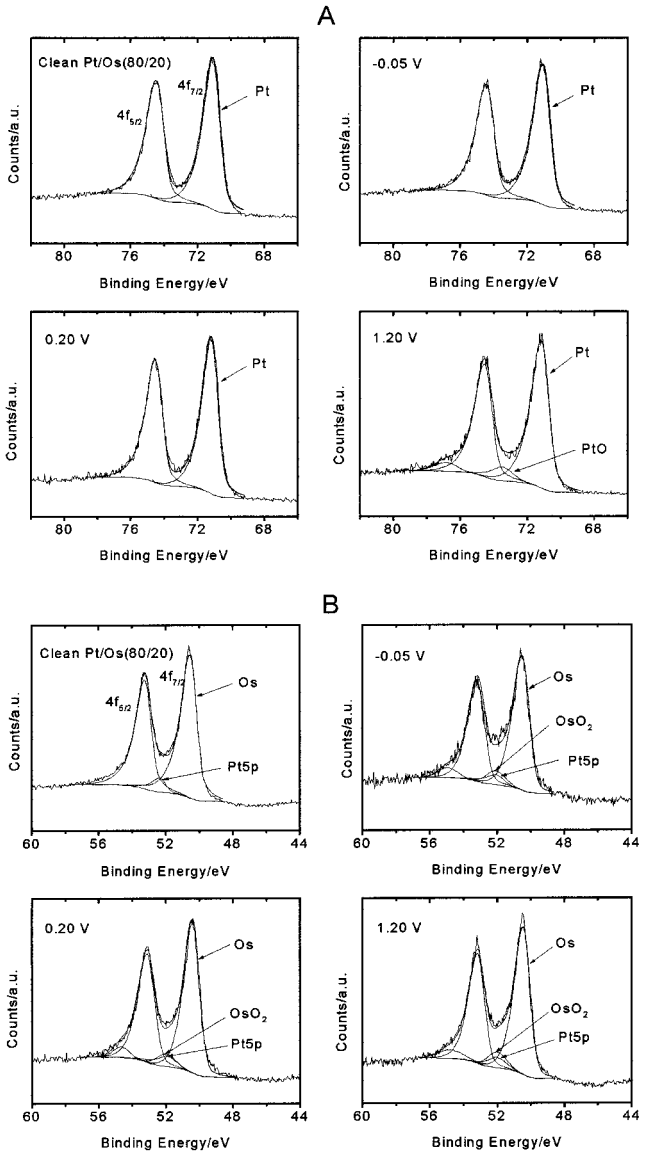

Figure 3. X-ray photoelectron spectra of (A) platinum and (B) osmium species from the Pt/Os (80/20) surface at several electrode potentials in 0.5 M H_2SO_4. The doublet for metallic osmium appears at 50.4 ($4f_{7/2}$) eV and at 53.1 eV ($4f_{5/2}$). The doublet for OsO_2 is at 51.9 eV ($4f_{7/2}$) and at 54.6 eV ($4f_{5/2}$). The Pt 5p (52.0 eV) level overlaps with the osmium spectra. Other details as in Figure 1.

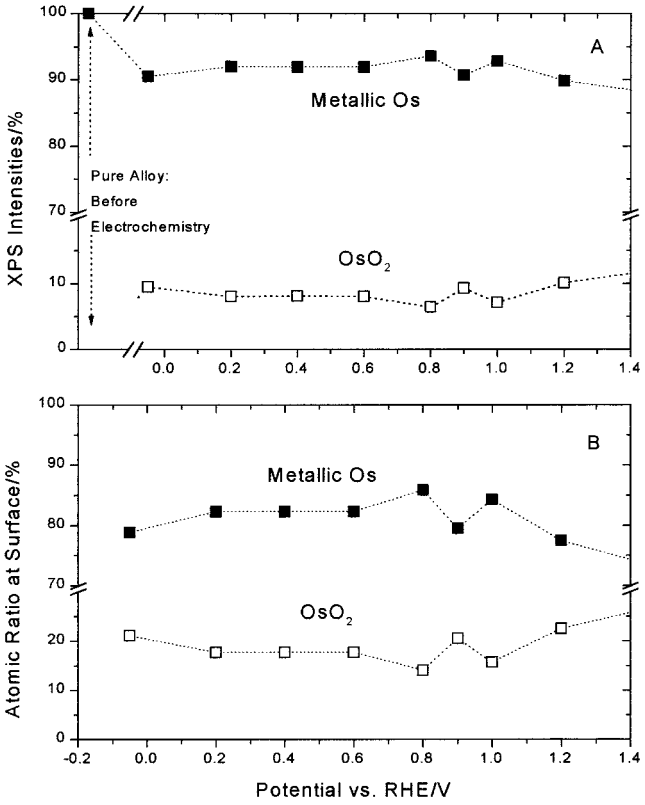

Figure 4. Potential dependency of (A) relative XPS peak intensity from metallic osmium and from OsO_2 on the Pt/Os (50/50) surface (from data such as shown in Figure 3), and (B) atomic ratios of metallic osmium and OsO_2.

TABLE 3: Atomic Ratio of Pt/Os (80/20) Alloy at Surface Region vs Electrode Potential

potential (V vs RHE)	Pt (%)	Os (%)
no potential (before electrochemistry)	80.8	19.2
−0.05	83.1	16.9
0.2	82.1	17.9
0.4	81.9	18.1
0.6	85.2	14.8
0.8	84.5	15.5
0.9	84.8	15.2
1.0	82.9	17.1
1.2	85.4	14.6
1.4	84.7	15.3

Table 3 includes the atomic ratio of Pt and Os at the surface vs electrochemical potentials. Before electrochemical treatment the XPS analysis shows slight Pt enrichment at the alloy surface. However, after electrochemical treatment, Pt further segregates to the surface.

XPS of Arc-Melted PtRuOs(65/25/10) Electrode. The XPS spectrum of arc-melted PtRuOs (Figure 5) consists of several major lines that are predicted from pure Pt, Ru, and Os, respectively. Figure 6, parts A, B, and C shows the potential-dependent XPS of Pt 4f, Ru 3d, and Os 4f core-levels. Electrochemical treatment of the Pt/Ru/Os alloy introduces oxygenated species. The BE assignments of the electrochemically generated oxides are consistent with of RuO_2, RuO_3 (Figure 6B) and OsO_2 (Figure 6C). The existence of oxide species is confirmed by the positions of XPS spectra as shown above and in Table 1. No additional oxide species on the ternary alloy surfaces are suggested by the spectra. However, this does not exclude the possibility of OsO_4 formation since this material is a gas and may not be detected in UHV conditions.

Plots of the relative intensities of the Ru 3d and Os 4f lines of the surface oxides and the clean metal as a function of potential are given in Figure 7A. In Figure 7B, the intensities have been used to quantify the distribution of oxides on the surface. Upon electrochemical treatment of the clean PtRuOs alloy, the relative amounts of surface oxides continue to increase up to 0.8 V. Interestingly, the ratio of Os oxide was higher on the ternary than on PtOs alloy, and the Ru oxides on the ternary were decreased in comparison with the PtRu alloy (see Figure 7B). Table 4 shows the Pt, Ru, and Os surface (monolayers) concentrations, calculated from XPS spectra using eq 1, as a function of the potential for PtRuOs alloy. Before electrochemical treatment, the surface composition is very similar to the bulk structure. After electrochemical treatment, the surface becomes enriched with platinum as it did in the PtRu and PtOs binary alloys.

Potential-Dependent IRAS of Alloy Electrodes. Figure 8 shows the CVs of CO-dosed Pt electrodes swept from the adsorption potential, 0.05 V, to 0 V followed by two cycles (0

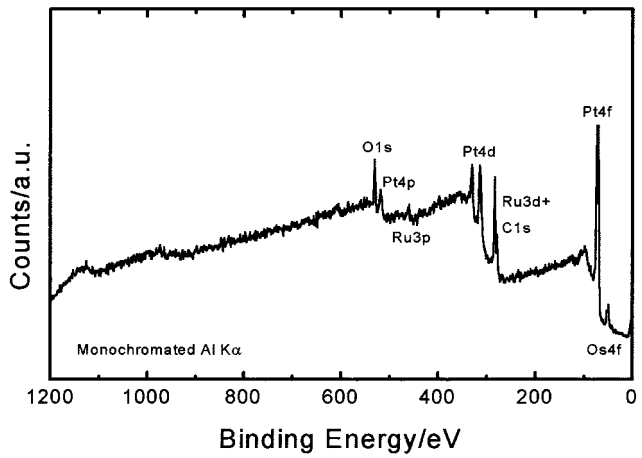

Figure 5. A wide-range XPS spectrum from the Pt/Ru/Os (65/25/10) electrode to demonstrate the presence of Pt, Ru, and Os. Other details as in Figure 1.

V to 1.4 V). On the first positive scan, the hydrogen oxidation charge integral (Q_H^{CO}) is diminished by the presence of CO_{ads}. At sufficiently positive overpotentials, the CO_{ads} is oxidized. On the second positive scan, a hydrogen oxidation charge integral (Q_H^H) is obtained in the absence of CO_{ads}. The CO coverage, θ_{co}, is defined as $(Q_H^H - Q_H^{CO})/Q_H^H$. The CVs of Pt in 0.5 M H_2SO_4 dosed with 50%, 1%, and 0.1% CO-balanced Ar, respectively, yielded calculated CO coverages of 100.0%, 92.5%, and 68.2%, respectively.[76] The Ψ ($\Psi = Q_{CO}/(Q_H^H - Q_H^{CO})$) values are approximately 2 in all cases, suggesting linearly bonded CO.[77]

Figure 9 shows the IRAS of linearly bonded CO, (dosed with 50% CO) on Pt, PtRu(1/1), PtRuOs(65/25/10), PtRu(8/2), PtOs-(8/2), PtRuOs(8/1/1), and Ru electrodes in 0.5 M H_2SO_4, versus potential. The CO_{ads} band centers, $\bar{\nu}_{CO}$, on Pt and the Pt-based alloys initially increase linearly with electrode potential. At about 0.50 V on Pt and 0.40 V on both PtRu(1/1) and PtRuOs(65/25/10), the trend gradually reverses, and then abruptly shift to lower frequencies, coincident with a large decrease in the absorption integrals as the CO coverage is oxidatively diminished. Also, the bandwidths increase as the mole fraction of Pt is decreased.

Figure 10 shows the $\bar{\nu}_{CO_{ads}}$ of linearly adsorbed CO dosed, at fixed times, with (a) 50%, (b) 1%, and (c) 0.1% CO on Pt, PtRu(1/1), PtRu(8/2) PtOs(8/2), PtRuOs(8/1/1), PtRuOs(65/25/10), and Ru electrodes versus potential. CO_{ads} is not detectable on Ru when dosed with 1% or 0.1% CO. The $\bar{\nu}_{CO}$ shift to lower wavenumbers as the CO coverage is reduced, and as the mole fraction of Pt is decreased under constant dosing conditions. The slope of the linear region (i.e., constant coverage region) for Pt, $(\partial\bar{\nu}/\partial V)_{Pt}$, significantly increases with decreasing θ_{co} in contrast to $(\partial\bar{\nu}/\partial V)_{alloys}$, which shows less dependence on the CO coverage but are steeper than for pure Pt.

Figure 11 shows the normalized[78] peak areas of linear CO_{ads} on Pt, PtRu(1/1), PtRu(8/2), PtOs(8/2), PtRuOs(8/1/1), PtRuOs-(65/25/10), and Ru electrodes in 0.5 M H_2SO_4 dosed with 50%, 1%, and 0.1% CO versus electrode potential. The onset potential for CO oxidation indicated by the decrease of the CO peak integrals are Pt > $Pt_{80}X$ (X is either Os or Ru) > $Pt_{50}Ru_{50}$ > $Pt_{65}Ru_{25}Os_{10}$ as shown in Figure 11a,b, and c. Figure 12 shows the potential dependence of the bandwidth at half-height of linearly adsorbed CO on Pt dosed with 50%, 1%, and 0.1% CO: the bandwidths increase as the CO coverage is decreased.

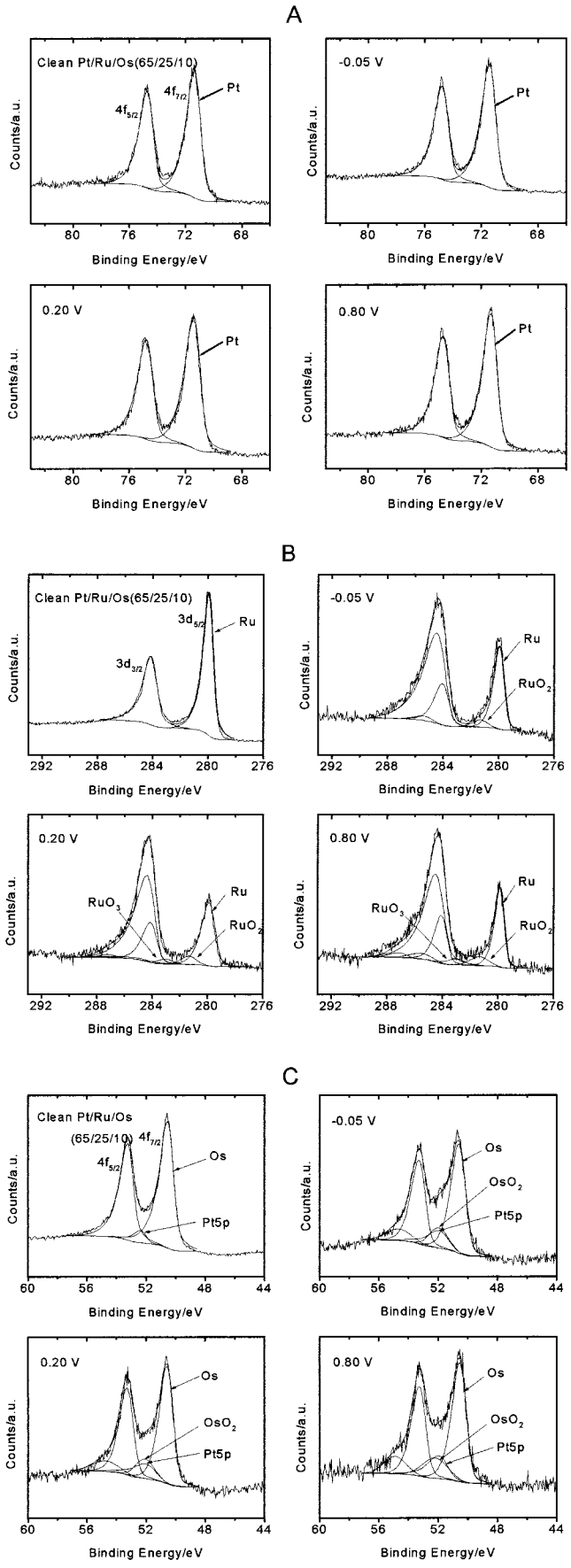

Figure 6. X-ray photoelectron spectra from the Pt/Ru/Os (65/25/10) surface: (A) for the Pt species, (B) for the Ru species, and (C) for the Os species. Other details as in Figure 1.

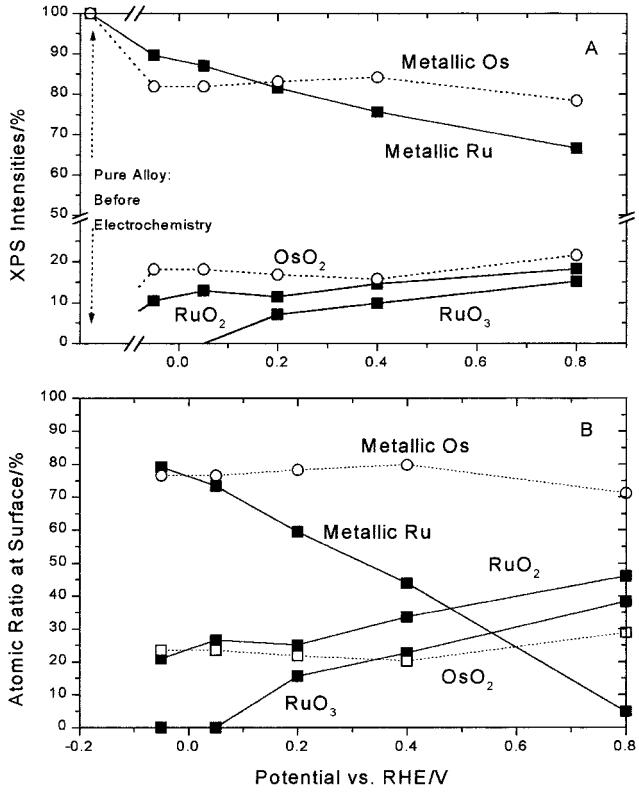

Figure 7. (A) Potential dependency of peak intensities from X-ray photoelectron spectra of the Ru and Os species on the Pt/Ru/Os (65/25/10) surface. (B) Atomic ratios of the Ru and Os species in different oxidation states as a function of the electrode potential. For brevity, the oxidation states are denoted as oxides. See also Figure 6.

TABLE 4: Atomic Ratio of Pt/Ru/Os (65/25/10) Alloy at Surface Region vs Electrode Potential

potential (V vs RHE)	Pt (%)	Ru (%)	Os (%)
no potential (before electrochemistry)	66.0	25.7	8.3
−0.05	71.0	20.7	8.3
0.05	71.2	20.0	8.8
0.2	68.0	24.1	7.9
0.4	68.0	23.9	8.1
0.8	69.2	21.8	8.9

Discussion

Oxidation States and Surface Composition of Alloy Electrodes. The XPS data summarized in Figures 2 and 4 confirm a broad potential window where both Ru and Os exist as a distribution of oxides, while Pt is entirely metallic. Two Ru states and one Os state have positive chemical shifts of 1.3, 2.8, and 1.5 eV versus the metallic states of Ru and Os, respectively (Table 1). The spectra confirm that the active oxygen required for CO oxidation is formed at the second metal rather than at a Pt site in binary and ternary catalysts. Ruthenium exists as both Ru^{4+} and Ru^{6+} at potentials above 0.20 V in the binary and ternary alloys. These oxides may serve as the source of oxygen required for the methanol oxidation reaction. In both the PtOs and PtRuOs alloys we detect only one oxidation state for Os; the tetra-oxide was not observed. In addition to the promoting effects of Ru and Os,[1−13] the stability of RuO_2/RuO_3 and OsO_2 on the electrode surface is an important factor.

Quantification of the applied-potential-dependent surface coverages of the Ru and Os oxides sheds light on the applicability of the bifunctional mechanism and interpretation of the IRAS of adsorbed CO. We have shown that RuO_x species and OsO_2 are prevalent within the potential window required for DMFCs. Os is partially oxidized even at −0.05 V. Below +0.05 V, RuO_2 has about 25% coverage on Pt/Ru(1/1) which means half of Ru is oxidized (Figure 2B). At 0.20 V, the coverage includes 30% RuO_2, 15% RuO_3, and 5% metallic Ru up to 0.60 V. Ru sites are completely oxidized above 0.80 V. The PtOs(8/2) electrode has 20−25% of the Os oxidized over the whole potential range, including −0.05 V (Figure 4B). On the PtRuOs(65/25/10) alloy, increased OsO_2 (25−30%) and reduced RuO_x (25−45% of RuO_2) formation were observed (Figure 7B). This may be related to modification of the electronic structure (and the adsorptive properties) at ternary alloys by electron transfer from Ru to Os. At 0.20 V, the total surface oxide coverage is 45% on PtRu(1/1), 4% on PtOs(8/2), and 12% on PtRuOs(65/25/10). Thus 90%, 20%, and 33% of the alloying metals on PtRu, PtOs, and PtRuOs, respectively, are oxidized at 0.20 V in sulfuric acid solution while Pt is entirely metallic. The alloying metals are oxidized within the potential window of operating fuel cells (Os is partially oxidized even at −0.05 V) and probably play the role of oxygen transfer agents in a bifunctional mechanism for methanol oxidation. The large differences in surface coverages of oxide species, however, render the relationship of extent of surface oxidation to activity of catalysis somewhat complicated. It is quite possible that in ternaries, the relative roles of the oxophilic Ru and Os components toward water activation are potential dependent. The dynamic role of oxide species (transport issues) as well as electronic properties must also be considered. Finally, more exact surface coverage and ruthenium valency determination requires better models of the surface structure.[58]

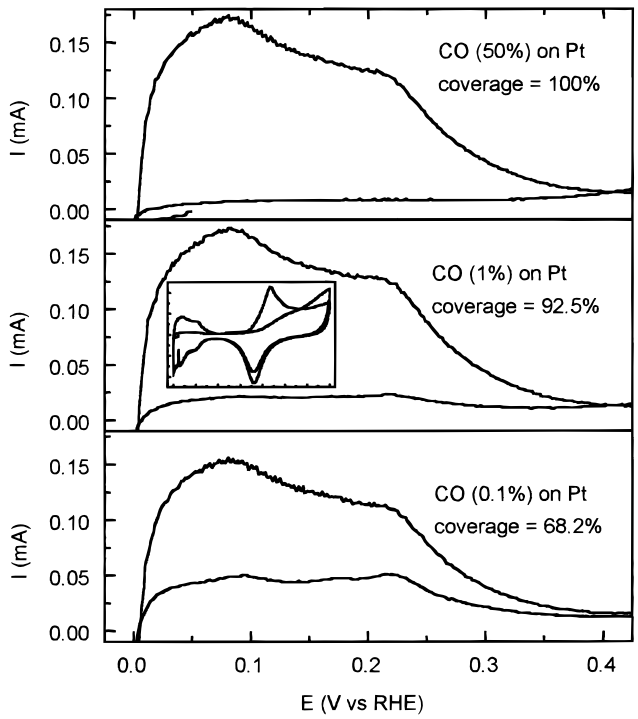

Figure 8. CVs for CO_{ads} stripping on Pt electrode.

Surface segregation in binary alloys has been studied.[79] The catalytic activity of alloys depends on the surface composition, which can vary considerably from that of the bulk. Although we observed no significant segregation after UHV treatment (sputtering, annealing), our XPS data confirm that the surface composition varies with potential in the electrochemical cell (Tables 2, 3, and 4). In general, the surface enrichment suggests sufficient surface mobility of metal ions under potentiostatic control in the aqueous phase to cause surface segregation at

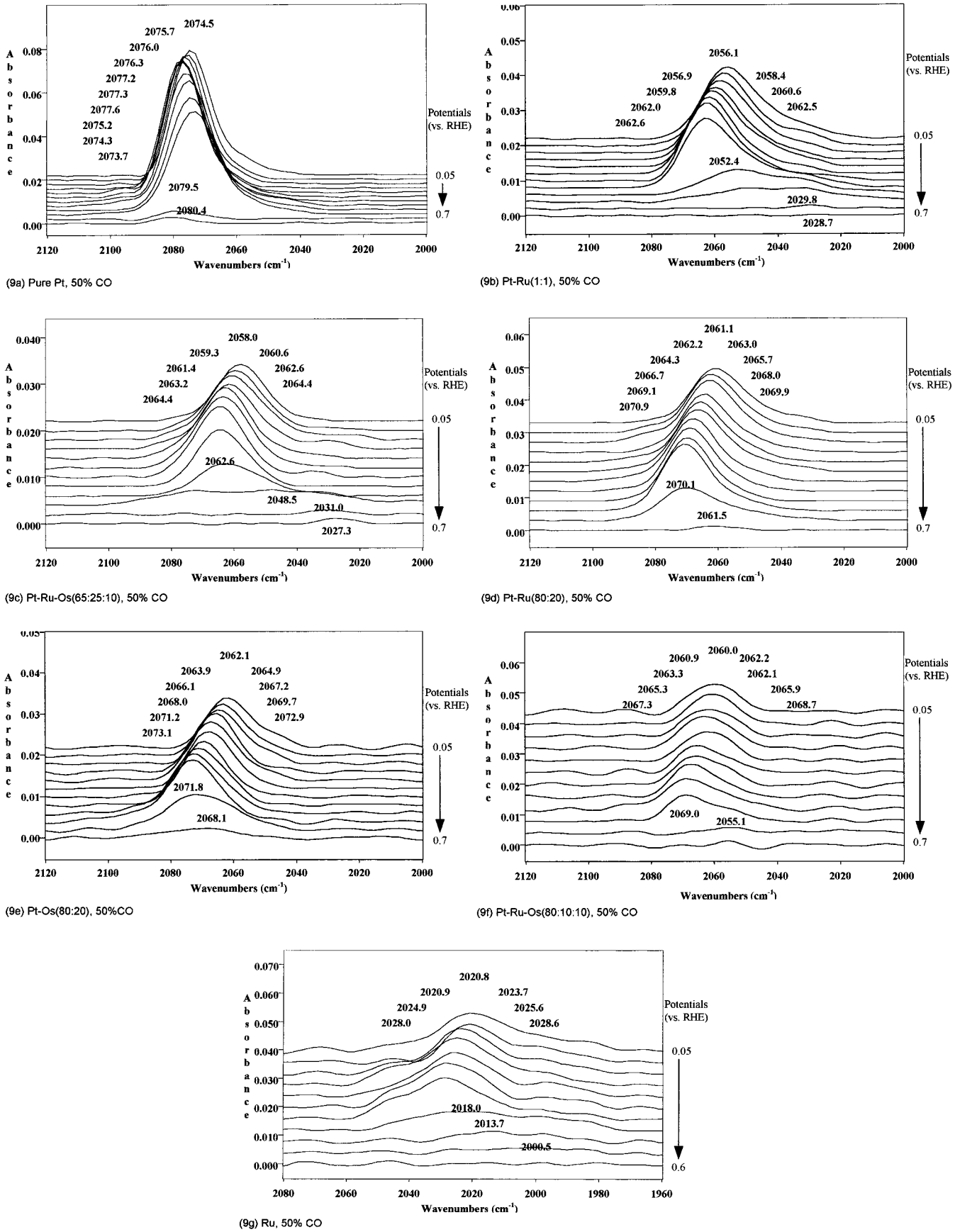

Figure 9. (a) Pure Pt, 50% CO; (b) Pt−Ru(1:1), 50% CO; (c) Pt−Ru−Os(65:25:10), 50% CO; (d) Pt−Ru(80:20), 50% CO; (e) Pt−Os(80:20), 50% CO; (f) Pt−Ru−Os(80:10:10), 50% CO; (g) Ru, 50% CO; (a−g) PEM-FTIR spectra (50% CO on Pt, Pt alloys, and Ru).

room temperature. In most cases, given similar sizes, the metal having the lower heat of sublimation tends to surface segregate (Pt, Ru, and Os atomic radii are 1.39, 1.34, and 1.35 Å). The heats of vaporization of Pt, Ru, and Os are 135.1, 153.6, and 189.0 kcal/mol, respectively,[80] suggesting surface enrichment of Pt.[81,82] Our XPS data confirm this on all three alloys. Binary

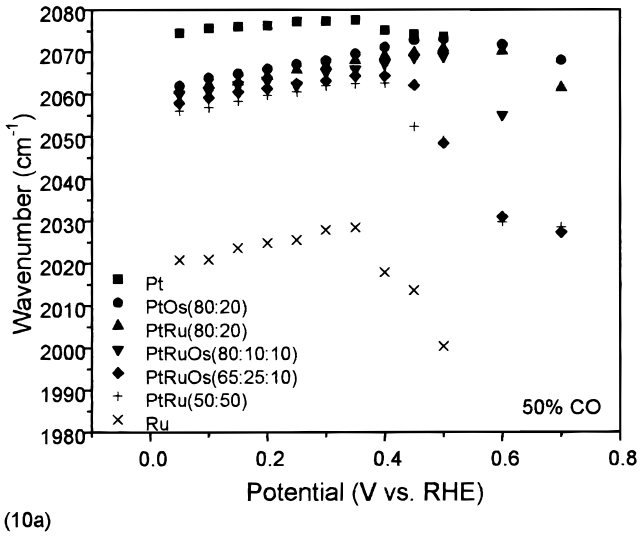

(10a)

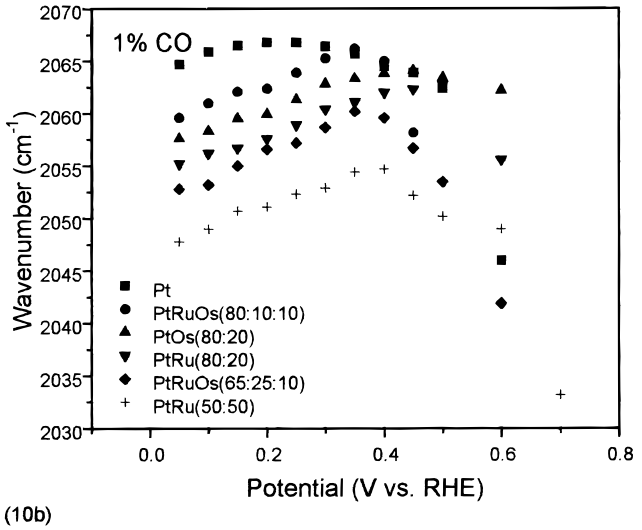

(10b)

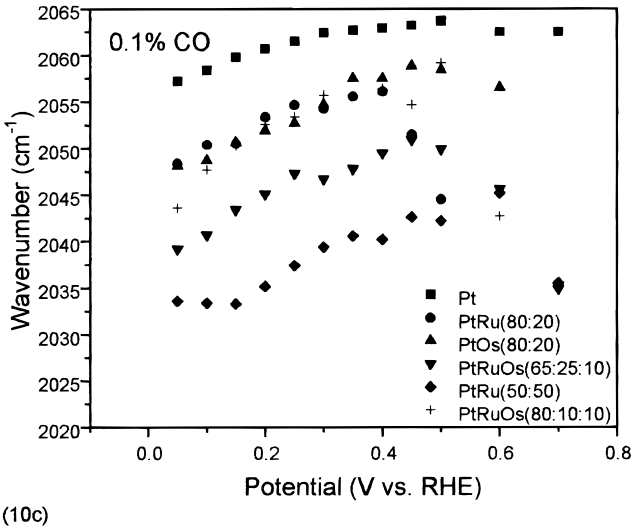

(10c)

Figure 10. Wavenumber vs potential for different electrodes dosed with different CO concentration: (a) 50%CO, (b) 1% CO, (c) 0.1% CO.

PtRu (1/1) alloy surfaces are known to be resistant to Pt-enrichment caused by preferential Ru dissolution, up to ca. 1 V,[83] and the Os-containing alloys are stable up to 0.8 V.[15] At the highest potentials Ru can be lost as volatile RuO_4, and Os as volatile OsO_4 through corrosion.[84,85] It is known that X_{Pt} at

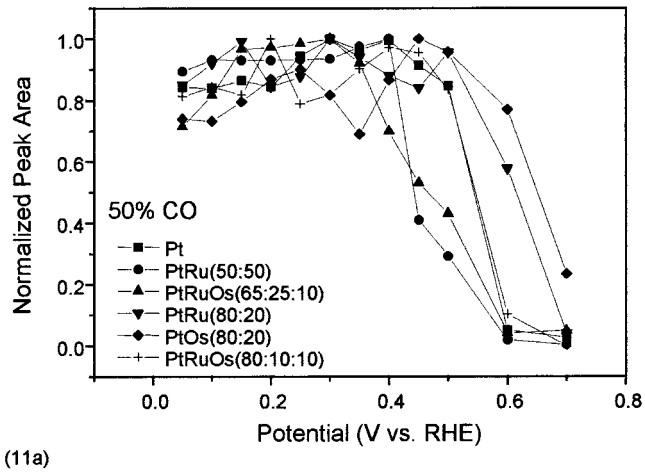

(11a)

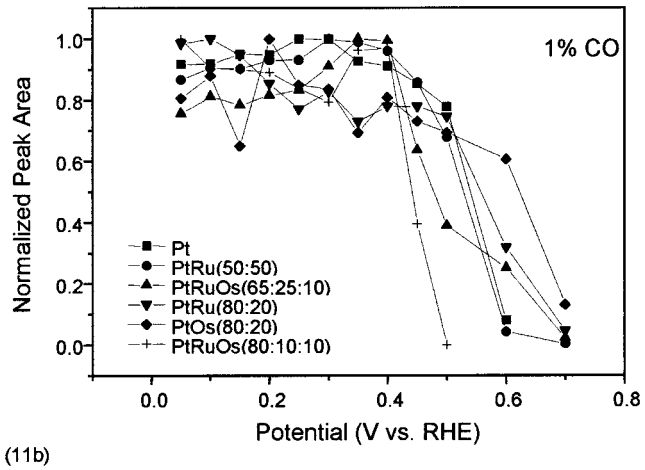

(11b)

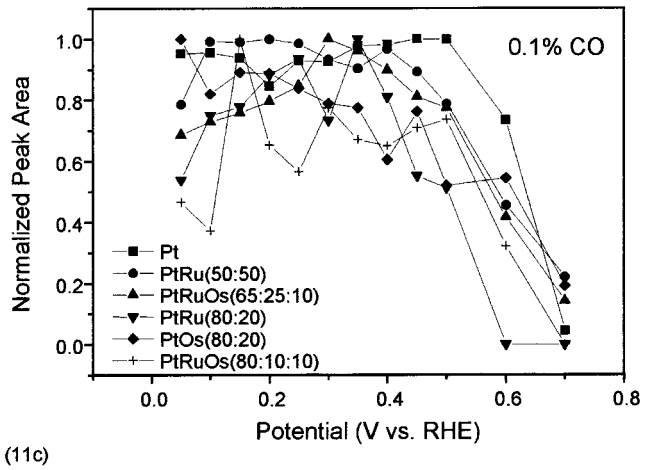

(11c)

Figure 11. Normalized peak areas vs potential: (a) 50%CO, (b) 1%CO, (c) 0.1% CO.

the surface in UHV is higher than in the solution.[86] Our segregation data may include changes during the UHV transfer since there is some Pt enrichment after sputtering with argon ions at 2 kV. Additional effects such as metal interactions with the chemisorbed adlayer or electrolyte may also play an important part in modifying the composition of the surface layer, and this is the subject of a study in progress. Interestingly, the XPS suggest minimal segregation at the alloy surfaces. Thus, interpretation of the IRAS to be discussed next can be done with the approximation that, in the case of arc-melted alloys, the elemental composition of the surface is essentially an extension of the bulk.

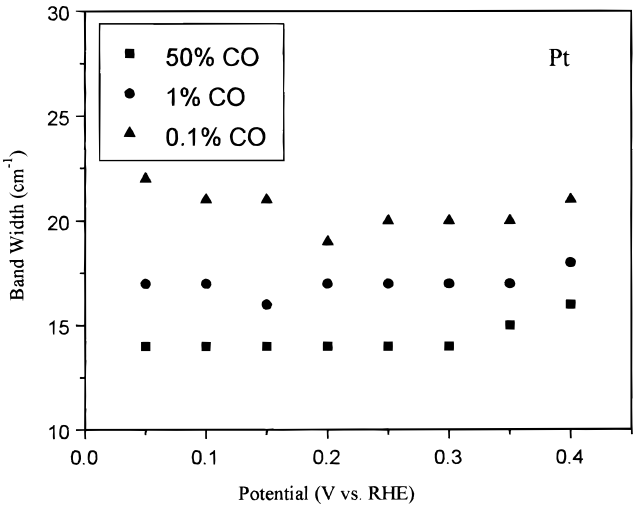

Figure 12. Bandwidth at half height of linearly adsorbed CO on Pt-dosed with 50%, 1%, and 0.1% CO at different potentials.

Potential-Dependent IRAS of linearly bound CO. *Background*. Understanding the effect of alloying on the linearly bound $\bar{\nu}_{CO}$ requires interrelated considerations such as (1) changes in the metal to $2\pi^*$ back-donation; (2) coverage effects (e.g., assuming that CO binds to platinum in preference to Ru, the overall CO coverage would diminish as the surface Pt mole fraction is decreased), and (3) relaxation effects (Pt−Pt bonding at the surface may be relaxed at the expense of stronger Pt−Ru bonding).[87] Consider the effects of ϵ_d shifts in light of the Blyholder's[88] model for CO bonding to metals. The metal-to-CO bonding involves donation from the 5σ MO of CO into the metal, and back-donation from the metal d-bands into the $2\pi^*$ MO of CO. The validity of the Blyholder model has been subject to many investigations. For example, periodic density functional theory calculations concerning the chemisorption of CO on Pd-(110)[89] suggests that the Blyholder model is too simplistic, and that 4σ and 1π MOs should be included in the model. A more recent study by Aizawa[90] used total energy calculations and a newly developed population analysis scheme that can be applied to wave functions expanded with a plane wave basis set. Aizawa's calculations showed that 4σ and 1σ MOs are completely filled and hence do not play a role in the bonding of CO to the surface, thus confirming the Blyholder picture.

In a model describing the interaction between the CO molecule and the metal d states, Nørskov describes the π bonding of CO to platinum in two steps.[91,92] In the first step, the $2\pi^*$ and the 5σ MOs are shifted down in energy and broadened due to coupling with the Pt s,p electrons. The renormalized CO orbitals are then mixed with the Pt d-band resulting in the splitting of the $2\pi^*$ MO into antibonding and bonding orbitals. This model rationalizes the experimental results by J. A. Rodriguez and D. W. Goodman[93] showing a correlation between the CO chemisorption energy and the surface core level shift.

The constrained space orbital variation (CSOV) methods,[94−96] used by Illas[97] and Fernandez-Garcia,[98] to study binding between CO and Pt clusters suggest that the wall effect, resulting from the Pauli principle (four electron interactions), is a significant contributor to the diminution of the CO stretching frequency upon chemisorption to platinum. Contrary to common belief, σ donation also was found to contribute negatively to the shift in the CO stretching frequency. A shift of the surface d-band center to more negative potentials increases overlap between the surface d-band and the renormalized $2\pi^*$ MO of CO. The surface d-band center of Pt can be affected by adjusting the potential of the surface electrochemically (Stark effect[99]) and/or by alloying the Pt. Nørskov's DFT calculations show that when smaller elements are alloyed into, or incorporated as adatoms with Pt, the d-band center shifts up. More recently, Nørskov[100] showed that the surface reactivity (adsorption of O and CO, and the dissociation of CO on strained and unstrained Ru(0001) surfaces) increases with lattice expansion, which is also explained by an upshift of the metal d states. Coverage effects, affecting infrared band centers and bandwidths, include vibrational coupling in the form of spatial dipole−dipole interactions and/or through-metal coupling.[101−104]

Absence of RuC−O Peaks on Alloys. Friedrich et al.[105] reported an infrared study of CO on Pt electrodes modified with Ru deposits. The CO stretching frequency on both Pt and Ru was observed at 2070 and 2010 cm^{-1}, respectively. The RuC−O stretching frequency was shown to be dependent on the Ru coverage. Ru adatoms on single crystal or Pt facets are arranged as surface islands;[106] the size of the islands is directly related to the Ru coverage.

In the case of alloys, the distribution of the alloying element (Ru and/or Os) is more uniform on the surface and no evidence of island formation is seen. XRD (bulk) and XPS data suggests more uniform distribution of the different elements constituting the alloy, even for PtRu (50/50). The absence of CO on Ru or Os spectral bands for the alloys can be attributed to a combination of different effects: (a) the electronic structure of Ru and Os in the alloy systems is different from island deposits. This is due to the difference in the nature of the close neighbors and to the difference in the surface strains. Strain effects should be more pronounced for systems with large misfit as in the case of adlayers. In fact, calculations show that strain modifies the electronic structure[107] and this can be the dominant effect.[108] In the arc-melted alloys, Ru and Os loose their identity in the platinum FCC matrix. This is reflected in the observed CO stretching frequency, being lower than the value obtained for pure Pt, and diminishing as the amount of the alloying component is increased. As already mentioned, this diminution can also be explained by an overall diminution of the total CO coverage on the surface, in which case, very little CO chemisorption on Ru or Os occurs. (b) The uniform distribution of the different elements on the surface favors the preference of CO toward chemisorption on Pt rather than on Ru or Os, and inversely OH to Ru and Os rather than to Pt. (c) Dipole−dipole interaction, stronger on the alloys, will on the other hand contribute to the screening effect of the spectral band of CO on Ru or Os by the higher CO vibrational frequency on Pt. An excellent example of this was demonstrated by Goodman[109] in the case of CO/Cu/Pt, showing a total attenuation of the Pt−CO signal for Cu coverage beyond 0.65 ML. Finally, we report in this work that for pure Ru, a relatively high CO dosage (50%) is required in order to observe the CO spectral band, in contrast to the alloys and pure Pt surfaces, where low CO dosage (0.1%) is sufficient to observe the CO spectral band.

Stark Tuning Rates. The Stark effect links variation of an electric field to vibrational frequencies of adsorbed molecules.[110−111] The chemical-bonding explanation for the potential dependence of $\bar{\nu}_{CO}$ was proposed by Anderson[113] for the CN on Ag, and later for CO adsorbed on Pt.[114] An increase in the potential reduces the occupancy of the CO $2\pi^*$ molecular orbital,[115] increasing the CO bond order and the $\bar{\nu}_{CO}$. A variety of explanations relating CO stretching frequencies to Pt electrode potentials essentially correlate with the occupancy of the CO $2\pi^*$ MOs.[116,117] In addition to the chemical-bonding explanation

of the Stark effect, there is a purely electrostatic explanation (vibrational Stark effect), based on the change of the dipole moment of the adsorbed molecule in response to changes in the applied electrostatic field.[118] Changes in the CO bond order induced by d-band center shifts, as well as the vibrational Stark effect, contribute to observed linear Stark effects.[110,119] The Figure 10 series shows that the STRs for Pt, $(\partial\bar{\nu}/\partial V)_{Pt}$, significantly increase from 9.79 to 23.80 cm^{-1}/V as the coverage decreases from 100% to 68%. An increase in the STR as the coverage decreases has been observed in both vacuum and electrochemical experiments.[120] We believe that the increase in the STR is a result of a decrease in the renormalized $2\pi^*$ MO density of states as the coverage is decreased. Thus there are less $2\pi^*$ MOs competing for d-band electrons and $\bar{\nu}_{CO}$ becomes more sensitive to changes in the Fermi level, which indirectly affects overlap of the surface d-band with the renormalized adsorbate bands.

The alloy Stark tuning rates $(\partial\bar{\nu}/\partial V_{alloys})$ dosed under conditions that yield 100% coverage on pure Pt, range between 21 and 24 cm^{-1}/V. These values are similar to $(\partial\bar{\nu}/\partial V)_{Pt}$ dosed with 0.1% CO (68% coverage on pure Pt). Pt has the highest affinity for CO among the alloy components. Even if the CO coverage on the surface Pt of the alloy is 100%, the overall coverage would be reduced as the mole fraction of Pt on the surface is lowered. Thus, reduced dipole−dipole coupling would broaden the peaks and shift the peaks to lower wavenumbers as the Pt mole fraction is reduced. We observe this experimentally. The coverage on pure Pt was 68% when dosed with 0.1% CO. The Pt alloy mole fractions in this study vary from 80 to 50 mole percent. Thus the coverage regime obtained by varying the dosing conditions are bracketed by the variation of the alloy Pt mole fractions studied. Recall from our XPS data that there is no significant segregation at the alloy surfaces. This information combined with the fact that the STR lines systematically drop to lower frequencies as the mole fraction of Pt decreases suggest that there is no significant island formation and that the metal components are evenly distributed. Thus, the combination of XPS and IRAS suggests that the arc-melted alloy surfaces of this study do not deviate significantly from the bulk alloy structure. If significant segregation of Pt at the surface occurred along with Pt island formation, dipole−dipole interactions at the surface would be maintained on the Pt island regions and the effect of reduced overall coverage would be masked. In summary, *either* alloying or reduction of CO coverage on pure Pt would reduce the density of states of the 2 π^* MOs at the surface with similar reductions in dipole−dipole coupling in both cases. The reduction of the DOS of adsorbed species would reduce competition for d-band electrons, thus increasing back-donation of electrons to the $2\pi^*$ MOs of CO. The CO stretching frequencies would decrease, and the STRs increase as sensitivity to shifts in the d-band center increase with decreased competition for electrons. Figure 13 summarizes the $\bar{\nu}_{CO}$ data, at 50 mV, with variation of the Pt mole fraction and the CO dosing conditions. The $\bar{\nu}_{CO}$ decreases as either the mole fraction of the Pt is decreased under constant dosing conditions, or as the CO coverage is decreased at constant Pt mole fraction. The two parameters effecting variations of the band center frequencies—(1) alloying and (2) variation of coverage at constant composition—are related.

Alloying Stark Effect. In Figure 13, the solid circles, labeled in the legend as 50% CO, summarize the effect of alloying when dosing under conditions that yield 100 coverage on pure Pt. On Pt alloys, Pt is the preferred (though not exclusive) site over Ru for CO adsorption. We only observed CO adsorption on Ru at high CO dosing conditions (Figure 10). As the Pt mole fraction is reduced, the coverage goes down, but not linearly with mole fraction since at high coverages Ru adsorbs CO as well.

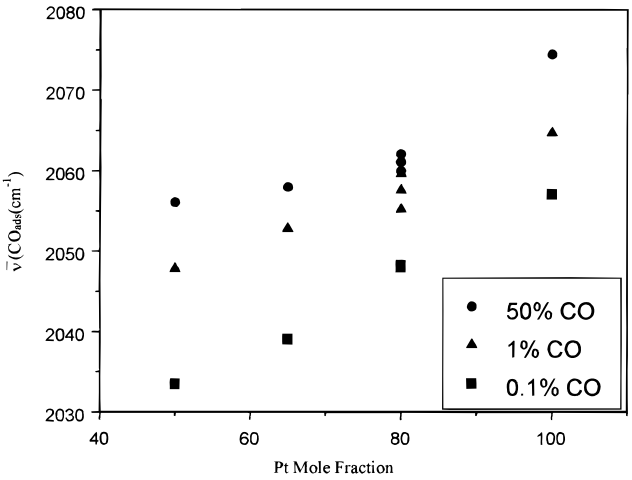

Figure 13. Wavenumber of CO adsorbed at 50 mV for 600 s vs Pt content.

The stretching frequencies diminish for two reasons, diminished dipole−dipole coupling, and as discussed earlier, reduced competition for back-bonding electrons. Since the coverage per surface atom is reduced on the alloys, the lower number of $2\pi^*$ MOs have less competition for d-band electrons. This would account for additional back-bonding and a further reduction in the stretching frequency. Recall (Figure 10) that we observed CO adsorption on Ru only when dosing with 50% CO. We could not detect CO adsorption on Ru when dosing with 1% or 0.1% CO. The triangles and squares in Figure 13 show effects due to the reduction of the CO dosing pressure in addition to changes in the Pt mole fraction. At a fixed mole fraction of Pt, the CO per Pt atom is decreased as the dosing pressure and time is decreased. This reduces dipole−dipole coupling which reduces the stretching frequencies. Additionally, Vanolli suggests that as the coverage is decreased, it is possible that CO migrates to more reactive sites resulting in a decrease of the stretching frequency.[121] The lower coverage results in less competition for d-band electrons, and there is increased back-donation. Figure 13 reveals another trend; as the mole fraction of Pt is reduced, the stretching frequencies are more sensitive to the variation of coverage due to changes in dosing conditions. When dosing with 0.1% CO (68% coverage on pure Pt), the stretching frequencies vary linearly with Pt mole fraction (solid squares in Figure 13). We call this the "alloying Stark effect". Further work using ^{13}CO is in progress to determine if the alloying Stark regime is a result of a linear electronic effect due to alloying. In summary, Figure 13 shows the effect of changes in dipole−dipole coupling due to reduced coverage with lower CO dosing pressures and times, superimposed upon an "alloying Stark effect."

Figure 14 shows the bandwidths of CO_{ads} $(\Delta\bar{\nu}_{CO})$ versus Pt mole fraction at 50 mV (solid line), and versus CO coverage on pure Pt (dashed line from Figure 14). On pure Pt, $\Delta\bar{\nu}_{CO}$ increases as CO coverage decreases. At constant CO dosing conditions, the $\Delta\bar{\nu}_{CO}$ increases as the Pt mole fraction is decreased. The band shape of CO_{ads} peaks on Pt is more symmetric and narrower than on the alloy surfaces dosed in the same manner. The broadening of CO adsorption peaks results from homogeneous and inhomogeneous contributions. The site distribution can be increased by lowering the coverage or by increasing the surface heterogeneity by alloying. The low

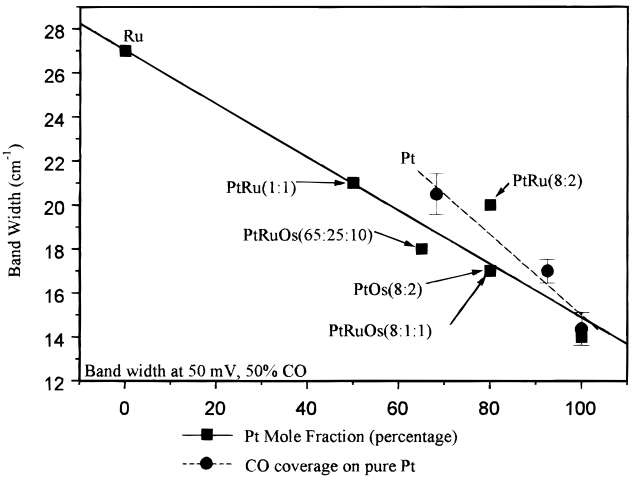

Figure 14. Bandwidths of CO_{ads} as a function of Pt mole fraction at 50 mV (solid line) and as a function of CO coverage on pure Pt (dashed line).

frequency tails have been attributed to inhomogeneously distributed surface adsorption sites.[101,122] A correlation between the bandwidths as a function of Pt mole fraction at high CO dosing pressures, and the bandwidths as a function of CO coverage on pure Pt is evident in Figure 14. Figure 14 shows that, in addition to the previously discussed downshift in the CO stretching frequency with alloying and/or a reduction in the CO partial pressure, there is an increase in the bandwidth as the Pt mole fraction and/or the CO dosing pressure decreases. If one assumes that CO adsorbs primarily on Pt atoms in the alloys, than even though the overall coverage is decreased as the mole fraction of the Pt is decreased, the CO coverage on the alloy Pt atoms could still be 100%. Thus the Pt mole fraction would be equivalent to the coverage if one assumes 100% coverage on the alloy Pt when dosing with 50% CO. Our data shows that there is adsorption of CO on pure Ru surfaces when dosed under conditions which result in complete coverage on pure Pt, but no detectable coverage on Ru when dosed under conditions that yield 68% coverage on pure Pt. However this must be interpreted with caution since pure Ru is hcp while the Pt alloys are fcc. The near overlap of the two lines of Figure 10 suggests that the assumption is not unreasonable. Consequently, we ascribe the reduction of the CO stretching frequency as the mole fraction of Pt is decreased to both an upward shift of the d-band and the result of decreased overall coverage.

Conclusions

We have correlated the coverage and potential-dependent infrared spectra of adsorbed CO on arc-melted Pt, PtRu(1/1), PtRu(8/2), PtOs(8/2), PtRuOs(8/1/1), PtRuOs(65/25/10), and Ru to the potential-dependent X-ray photoelectron spectra of the PtRu(1/1), PtOs(8/2), and PtRuOs(65/25/10) substrates. The alloy XPS data confirm that the Pt component is metallic at potentials relevant to fuel cell anode catalysts. Os and Ru are partially oxidized, even at −50 mV vs RHE, suggesting that the alloying additives act as oxygen transfer agents in a bifunctional mechanism. The XPS confirm that there is no significant segregation at the alloy surfaces. The observations of minimal surface segregation, and the systematic drop of the Stark Tuning Rate lines to lower frequencies as the mole fraction of Pt in the alloys is decreased, suggests that the alloy components are distributed evenly across the surface (i.e., no significant island formation occurs on the alloy surfaces). There is a systematic shift of the linear bound CO stretching frequencies to lower energies as the Pt content is reduced. Our explanation considers both coverage effects as well as changes in the electronic structure of the alloys.

At high-coverage CO dosing conditions, CO is adsorbed on Ru as well as on Pt. However since CO adsorbs on Pt in preference to Ru the overall coverage diminishes as the Pt content is reduced. The reduced dipole−dipole coupling shifts the stretching frequencies to lower energies and increases the bandwidths. On pure Pt, the bandwidths increase as the CO coverage is lowered. The increase of the bandwidths, along with the drop in CO coverage on pure Pt, parallels the bandwidth increase resulting from alloying at high CO dosing conditions. The link between these two relationships is the reduced overall coverage. Under low CO dosing conditions, where adsorption on pure Ru is not observed, the stretching frequencies decrease linearly with Pt mole fraction while the decrease is nonlinear at higher coverages. The nonlinearity probably results from concomitant CO adsorption onto the Ru.

The following sequence of events, we believe, accounts for the Stark tuning rate enhancements with alloying. As the overall CO coverage decreases on the alloys, the CO $2\pi^*$ density of states also decreases, thus reducing competition for back-bonded electrons. In turn, the reduced competition enhances the sensitivity of the CO bond order to changes in the electrode Fermi level energy, causing the Stark tuning rates to increase. There is a parallel between enhanced tuning rates resulting from the decrease in CO coverage on pure Pt, and enhanced tuning rates with alloying at high coverages. In both cases, we invoke a reduced competition for back-bonding electrons.

An electronic explanation for the alloy Stark effect that is consistent with the calculations of Nørskov and the assumption of electron transfer from the Ru to the Pt by Goodenough invokes increased back-bonding into the $2\pi^*$ MOs of the adsorbed CO as the Ru content is increased. We also observe this with Os. Only at the lowest CO dosing conditions, are the CO stretching frequencies linearly related to the alloy Pt mole fraction, and it is a low coverages that the effect of changes in dipole−dipole coupling could be minimized by effects due to changes in the electronic structure of the catalyst.

The onset potential for CO oxidation, indicated by the decrease of the CO peak integrals are Pt > PtX(8/2) > PtRu(1/1) > PtRuOs(65/25/10), where X is Ru or Os. This order does not coincide with the extent of oxide components at the surface as determined by our potential-dependent XPS data. Thus the role of Os in the electrocatalysis of methanol oxidation requires further investigation.

We are now conducting density functional theory calculations on CO adsorbed on alloys as well as $^{13}CO/^{12}CO$ spectroscopic studies to further isolate the effects of changes in the electronic structure from dipole−dipole coupling.

Acknowledgment. Funding was provided by Army Research Office grants DAAH04-94-G-0055, DAAH04-95-1-0570, and DAAG55-97-1-0198 administered by Illinois Institute of Technology and Department of Energy grant DEFG02-96ER45439 administered by the Frederick Seitz Materials Research Laboratory at the University of Illinois at Urbana−Champaign.

References and Notes

(1) Friedrich, K. A.; Geyzers, K.-P.; Stimming, U.; Stumper, J.; Vogel, R. Proton Conducting Membrane Fuel Cells. *The Electrochemical Society Proceedings Series*; Gottesfeld, S., Halpert, G., Landgrebe, A., Eds.; Pennington, NJ, 1995; PV 95−23, p 299.

(2) Sarangapani, S.; Lessner, P.; Kosek, J.; Giner, J.; Bae, I. T.; Scherson, D. Direct Methanol-Air Fuel Cells. *The Electrochemical Society*

Proceedings Series; Landgrebe, A. R., Sen, R. K., Wheeler, D. J., Eds.; Pennington, NJ, 1992; PV 92−14, p 161.
(3) Lamy, C.; Leger, J. M.; Clavilier, J.; Parsons, R. *J. Electroanal. Chem*. **1983**, *150*, 71.
(4) Parsons, R.; VanderNoot, T. *J. Electroanal. Chem*. **1988**, *257*, 9.
(5) Iwasita, T.; Xia, X. H.; Liess, H.-D.; Vielstich, W. *J. Phys. Chem. B* **1997**, *101*, 7542.
(6) Watanabe, M.; Vehida, M.; Motoo, S. *J. Electroanal. Chem.* **1987**, *229*, 395.
(7) Hamnet, A.; Kennedy, B. J. *Electrochim. Acta* **1988**, *33*, 1613.
(8) Troughton, G. L.; Hamnett, A. *Bull. Electrochem*. **1991**, *7*, 488.
(9) Gasteiger, H. A.; Markovic, N.; Ross, P. N.; Cairns, E. J. *J. Phys. Chem*. **1993**, *97*, 12020.
(10) Herrero, E.; Franaszczuk, K.; Wieckowski, A. *J. Electroanal. Chem.* **1993**, *361*, 269.
(11) Krausa, M.; Vielstich, W. *J. Electroanal. Chem.* **1994**, *379*, 307.
(12) Gasteiger, H. A.; Markovic, N.; Ross, P. N. *J. Phys. Chem*. **1995**, *99*, 16757.
(13) Hogarth, M. P.; Hards, G. A. *Plat. Met. Rev.* **1996**, *40*, 150.
(14) Frelink, T.; Visscher, W.; van Veen, J. A. R. *Langmuir* **1996**, *12*, 3702.
(15) Ley, K. L.; Liu, R.; Pu, C.; Fan, Q.; Leyarovska, N.; Segre, C.; Smotkin, E. S. *J. Electrochem. Soc.* **1997**, *144*, 1543.
(16) Chrzanowski, W.; Wieckowski, A. *Langmuir* **1997**, *13*, 5974.
(17) Chrzanowski, W.; Kim, H.; Wieckowski, A. *Catal. Lett*. **1998**, *50*, 69. Chrzanowski, W.; Kim, H.; Tremiliosi-Filho, G.; Wieckowski, A.; Grzybowska, B.; Kulesza, P. *J. New Mater. Electrochem. Sys.* **1998**, *1*, 31.
(18) Reddington, E.; Sapienza, A.; Gurau, B.; Viswanathan, R.; Sarangapani, S.; Smotkin, E. S.; Mallouk, T. E. *Science* **1998**, *280*, 1735.
(19) Anderson, A. B.; Grantscharova, E.; Seong, S. *J. Electrochem. Soc*. **1996**, *143*, 2075.
(20) Watanabe, M.; Uchida, M.; Motoo, S. *J. Electroanal. Chem*. **1987**, *229*, 395−406.
(21) Cahen D.; Ibers, J. A. *J. Cata.* **1973**, *31*, 369−371.
(22) Beden, B.; Leger J.-M.; Lamy, C. In *Modern Aspects of Electrochemistry*; Bockris, J. O'M., Conway, B. E., White, R. E., Eds.; Plenum Press: New York, 1992; Vol. 22, pp 97−247.
(23) Frelink, T.; Visscher, W.; van Veen, J. A. R. *Surf. Sci*. **1995**, *335*, 353.
(24) Ticanelli, E.; Berry, J. G.; Paffet, M. T.; Gottesfeld, S. *J. Electroanal. Chem.* **1989**, *258*, 61.
(25) Gasteiger, H. A.; Markovic, N.; Ross, P. N.; Cairns, E. J. *J. Phys. Chem.* **1993**, *97*, 12020.
(26) Watanabe, M.; Motoo, S. *J. Electroanal. Chem*. **1975**, *60*, 275.
(27) Jinang, X.; Permeter, J. E.; Estrada, C. A.; Goodman, D. W. *Surf. Sci*. **1991**, *249*, 44.
(28) Goodenough, J. B.; Manoharan, R.; Shukla, A. K.; Ramesh, K. V. *Chem. Mater*. **1989**, *1*, 391.
(29) Frelink, T.; Visscher, W.; van Veen, J. A. R. *Electrochim. Acta* **1994**, *39* (11), 1871.
(30) Iwasita, T.; Nart, F. C.; Vielstich, W. *Ber. Bunsen-Ges. Phys. Chem.* **1990**, *94*, 1030.
(31) Gasteiger, H. A.; Markovic, N.; Ross, P. N., Jr.; Cairns, E. J. *J. Electrochem. Soc.* **1994**, *141*, 1795.
(32) Gasteiger, H. A.; Markovic, N.; Ross, P. N., Jr.; Cairns, E. J. *Electrochim. Acta* **1994**, *39*, 1825.
(33) Gasteiger, H. A.; Markovic, N.; Ross, P. N.; Cairns, E. J. *J. Phys. Chem.* **1994**, *98*, 617.
(34) Watanabe, M.; Genjima, Y.; Turumi, K. *J. Electrochem. Soc.* **1997**, *144*, 423.
(35) Gurau, B.; Viswanathan, R.; Liu, R.; Lafrenz, T. J.; Ley, K. L.; Smotkin, E. S.; Reddington, E.; Sapienza, A.; Chan, B. C.; Mallouk, T. E.; Sarangapani, S. *J. Phys. Chem. B* **1998**, *102*, 9997.
(36) Hagans, P. L.; Swider, K. E.; Rolison, D. R. *Proc. Electrochem. Soc.* **1997**, *97*−*13*, 86.
(37) Rolison, D. R.; Hagans, P. L.; Swider, K. E.; Long, J. W. *Langmuir* **1999**, *15*, 774.
(38) Russell, J. W.; Overend, J.; Scanion, K.; Severson, M.; Bewick, A. *J. Phys. Chem*. **1982**, *86*, 3066−3070; Russell, J. W.; Severson, M.; Scanion, K.; Overend, J.; Bewick, A. *J. Phys. Chem.* **1983**, *87*, 293.
(39) Iwasita, T. In Tobias, C., Gerischer, H., Eds., *Advances in Electrochemical Science and Engineering*; VCH: Weinheim, **1990**; Vol. 1, p 127.
(40) Iwasita, T.; Nart, F. C. In *Advances in Electrochemical Science and Engineering;* Gerischer, H., Tobias, C. W., Eds.; VCH: Weinheim, 1995; Vol. 4, p 123.
(41) Kim, C. S.; Korzeniewski, C. *Anal. Chem*. **1997**, *69*, 2349.
(42) Kim, C. S.; Tornquist, W. J.; Korzeniewski, C. *J. Chem. Phys.* **1994**, *101*, 9113.
(43) Bastien, A. G. T. M.; Toolenaar, F. J. C. M.; Ponec, V. *J. Catal.* **1984**, *90*, 88.
(44) Lin, W. F.; Iwasita, T.; Vielstich, W. *J. Phys. Chem. B* **1999**, *103*, 3250.
(45) Hamnett, A.; Kennedy, B. J.; Wagner, F. E. *J. Catal*. **1990**, *124*, 30.
(46) Hable, C. T.; Wrighton, M. S. *Langmuir* **1993**, *9*, 3284.
(47) Kim, H.; Tremiliosi-Filho, G.; Wieckowski, A. In preparation.
(48) Soriaga, M. P.; Harrington, D. A.; Stickney, J. L.; Wieckowski, A. In *Modern Aspects of Electrochemistry*; Bockris, J. O'M., Conway, B. E., White, R. E., Eds.; Plenum Press: New York, 1996.
(49) Sung, Y.-E.; Thomas, S.; Wieckowski, A. *J. Phys. Chem*. **1995**, *99*, 13513.
(50) Thomas, S.; Sung, Y.-E.; Kim, H. S.; Wieckowski, A. *J. Phys. Chem.* **1996**, *100*, 11726.
(51) Han, M.; Mrozek, P.; Wieckovski, A. *Phys. Rev. B* **1993**, *48*, 8329.
(52) Shirley, D. A. *Phys. Rev. B* **1972**, *5*, 4709.
(53) Sherwood, P. M. A. In *Practical Surface Analysis*; Briggs, D., Seah, M. P., Eds.; Wiley: New York, 1990; Appendix 3.
(54) Moulder, J. F.; Stickle, W. F.; Sobol, P. E.; Bomben, K. D. *Handbook of X-ray Photoelectron Spectroscopy*; Chastin, J., Ed.; Physical Electronics: Eden Prairie, MN, 1992.
(55) Wagner, C. D.; Davis, L. E.; Zeller, M. V.; Taylor, J. A.; Raymond, R. M.; Gale, L. H. *Surf. Interface Anal*. **1981**, *3*, 211.
(56) Chan, R. W. M.; Kwok, R. W. M.; Lau, W. M.; Yan, H.; Wong, S. P. *J. Vac. Sci. Technol. A* **1997**, *15*, 2787.
(57) Tanuma, S.; Powell, C. J.; Penn, D. R. *Surf. Interface Anal.* **1991**, *17*, 911.
(58) Kim, H.; Tremiliosi-Filho, G.; Sung, Y.; Moraes, I. To be published.
(59) Kunimatsu, K.; Golden, W. G.; Seki, H.; Philpott, M. R. *Langmuir* **1985**, *1*, 245.
(60) Kunimatsu, K.; Seki, H.; Golden, W. G.; Gordon, J. G., II; Philpott, M. R. *Langmuir* **1986**, *2*, 464.
(61) In our previous work the electrodes were etched in dilute aqua regia at 25 °C for 10 s. We resorted to potential cycling instead of etching to avoid spectral interference by nitrate ions.
(62) Baer, Y.; Heden, P. F.; Hedeman, J.; Klasson, M.; Nording, C.; Siegbahn, K. *Phys. Scr*. **1970**, *1*, 55.
(63) Kim, K. S.; Winograd, N.; Davis, R. E. *J. Am. Chem. Soc.* **1971**, *93*, 6296.
(64) Johansson, G.; Hedman, J.; Berndtsson, A.; Klasson, M.; Nilsson, R. *J. Electron Spectrosc. Relat. Phenom*. **1973**, *2*, 295.
(65) Wittstock, G.; Strubing, A.; Szargan, R.; Werner, G. *J. Electroanal. Chem*. **1998**, *444*, 61.
(66) Tasaka, A.; Yachi, T.; Makino, T.; Hamano, K.; Kimura, T.; Momota, K. *J. Fluorine Chem.* **1999**, *97*, 253.
(67) Ramesh, K. V.; Sarode, V.; Vasudevan, S.; Shukla, A. K. *J. Electroanal. Chem*. **1987**, *223*, 91.
(68) McBreen, J.; Mukerjee, S. *J. Electrochem. Soc.* **1995**, *142*, 3399.
(69) Kim, K. S.; Winograd, N. *J. Catal*. **1974**, *35*, 66.
(70) Kötz, R.; Lewerenz, H. J.; Stucki, S. *J. Electrochem. Soc*. **1983**, *130*, 825.
(71) Vukovic, M.; Valla, T.; Milun, M. *J. Electroanal. Chem.* **1993**, *356*, 81.
(72) Chan, H. Y. H.; Takoudis, C. G.; Weaver, M. J. *J. Catal*. **1997**, *172*, 336.
(73) Zanoni, R.; Carinci, V.; Abu-Samn, R. H.; Psaro, R.; Dossi, C. *J. Mol. Struct.* **1985**, *131*, 363.
(74) Folkesson, B. *Acta Chem. Scand*. **1973**, *27*, 187.
(75) Sarma, D. D.; Rao, C. N. R. *J. Electron Spectrosc. Relat. Phenom*. **1980**, *20*, 25.
(76) The surface with a calculated coverage of 100% probably has sites not capable of CO adsorption for steric or electronic reasons. However, we assume 100% coverage as a reference point for the lower coverage surfaces.
(77) Iwasita-Vielstich, T. Progress in the study of Methanol Oxidation by *In-situ*, *Ex-situ* and On-line Methods. *Advances in Electrochemical Science and Engineering*, Alkire, R. C., Gerischer, H., Kolband, D. M., Tobias, C. W., Eds.; VCH Berlagsgesellschaft mbH: Weinheim (Germany), 1990; Vol. 1, pp 127−170.
(78) Peak areas are normalized to the maximum FTIR spectrum peak area of CO_{ads} on each electrode.
(79) Hilaire, L.; Diaz Guerrero, G.; Legare, P.; Maire, G.; Krill, G. *Surf. Sci.* **1984**, *146*, 569.
(80) Lide, D. R.; Kehiaian, H. V. *CRC Handbook of Thermophysical and Thermochemical Data*; CRC Press: Boca Raton, FL, 1994.
(81) Richarz, F.; Wohlmann, B.; Vogel, U.; Hoffschulz, H.; Wandelt, K. *Surf. Sci.* **1995**, *335*, 361.
(82) Tsong, T. T.; Ren, D. M.; Ahmad, M. *Phys. Rev. B* **1988**, *38*, 7428.
(83) Ticanelli, E.; Beery, J. G.; Paffett, M. T.; Gottesfeld, S. *J. Electroanal. Chem*. **1989**, *258*, 61.
(84) Lewerenz, H. J.; Stucki, S.; Kötz, R. *Surf. Sci.* **1983**, *126*, 463.
(85) Colon, F.; Gonzalez, J. H. *J. Electroanal. Chem*. **1976**, *73*, 303.
(86) Richarz, F. *Surf. Sci*. **1995**, *335*, 361.
(87) Personal communication. Matthew Neurock, University of Virginia, Department of Chemical Engineering.
(88) Blyholder, G. *J. Phys. Chem*. **1964**, *68* (10), 2772.

(89) Hu, P.; King, D. A.; Lee, M.-H.; Payne, M. C. *Chem. Phys. Lett*. **1995**, *246*, 73−78.
(90) Aizawa, H.; Tsuneyuki, S. *Surf. Sci.* **1998**, *399*, L364−L370.
(91) Hammer, B.; Nielsen, O. H.; Nørskov, J. K. *Catal. Lett.* **1997**, *46*, 31.
(92) Hammer, B.; Morikawa, Y.; Nørskov, J. K. *Phys. Rev. Lett*. **1996**, *76* (12), 2141.
(93) Rodriguez, J. A.; Goodman, D. W. *Science* **1992**, *257*, 897.
(94) Bagus, P. S.; Herman, K.; Bauschlicher, C. W. *J. Chem. Phys.* **1984**, *80*, 4378.
(95) Bagus, P. S.; Herman, K.; Bauschlicher, C. W. *J. Chem. Phys.* **1984**, *81*, 1966.
(96) Bagus, P. S.; Illas, F. *J. Chem. Phys.* **1992**, *96*, 8962.
(97) Illas, F.; López, N.; Ricart, J. M.; Clotet, A.; Conesa, J. C.; Fernandez-Garcia, M. *J. Phys. Chem. B* **1998**, *102*, 8017.
(98) Fernandez-Garcia, M.; Conesa, J. C.; Clotet, A.; Ricart, J. M.; López, N.; Illas, F. *J. Phys. Chem. B* **1998**, *102*, 141.
(99) Ianniello, R.; Schmidt, V. M.; Stimming, U.; Stumper, J.; Wallau, A. *Electrochim. Acta* **1994**, *39* (11/12), 1863.
(100) Mavrikakis, M.; Hammer, B.; Nørskov, J. K. *Phys. Rev. Lett.* **1998**, *81* (13), 2819.
(101) Moskovits, M.; Hulse, J. E. *Surf. Sci*. **1978**, *78*, 397.
(102) Hammaker, R. M.; Francis, S. A.; Eischens, R. P. *Spectrochim. Acta* **1965**, *21*, 1295.
(103) Severson, M. W.; Stuhlman, C.; Villegas I.; Weaver, Michael J. *J. Chem. Phys*. **1995**, *103*, 9832.
(104) Chang, Si-Chung; Weaver, M. J. *J. Chem. Phys.* **1990**, *92*, 4582.
(105) Friedrich, K. A.; Geyzers, K. P.; Henglein, F.; Marmann, A.; Stimming, U.; Unkauf, W.; Vogel, R. Electrode Processes VI. *The ECS Proceedings*; Wieckowski, A., Itaya, K., Eds.; The Electrochemical Society: Pennington, 1996; Vol. 96−98, p 119.
(106) Herrero, E.; Feliu, J. M.; Wieckowski, A. *Langmuir* **1999**, *15*, 4944.
(107) Behm, R. J., et al. *Surf. Science* **1998**, *411*, 249−262.
(108) Norskov, J. K. *Phys. Rev. Lett.* **1998**, *18* (N13), 2819.
(109) Goodman, D. W. *J. Phys. Chem.* **1992**, *96*, 7814.
(110) Lambert, D. L. *J. Chem. Phys*. **1988**, *89* (6), 3847.
(111) Villegas, I.; Weaver, M. J. *J. Phys. Chem.* B **1997**, *101*, 5842.
(112) Zou, S.; Weaver, M. J. *J. Phys. Chem.* **1996**, *100*, 4237.
(113) Anderson, A. B.; Kötz, R.; Yeager, E. *Chem. Phys. Lett*. **1981**, *82*, 130.
(114) Ray, N. K.; Anderson, A. B. *J. Phys. Chem*. **1982**, *86*, 4851.
(115) Mehandru, S. P.; Anderson, A. B. *J. Phys. Chem*. **1989**, *93*, 2044.
(116) Holloway, S.; Nørskov, J. K. *J. Electroanal. Chem*. **1984**, *161*, 193.
(117) Ueba, H. *Surf. Sci*. **1987**, *188*, 421.
(118) Lambert, D. K. *Phys. Rev. Lett*. **1983**, *50*, 2106, and **1983**, *51*, 2233 (E).
(119) Head-Gordon, M.; Hully, T. C. *Chem. Phys*. **1993**, *175*, 37.
(120) Hong, W.; Tobin, R. G.; Lambert, D. K. *J. Chem. Phys*. **1994**, *101* (5), 4277.
(121) Vanolli, F.; Heiz, D. K.; Schneider, W.-D. *Chem. Phys. Lett*. **1997**, *277*, 527.
(122) Persson, B. N. J.; Ryberg, R. *Phys. Rev. B* **1981**, *24*, 6954.